Title

Sustained ICP Elevation Is a Driver of Spatial Memory Deficits After Intraventricular Hemorrhage and Leads to Activation of Distinct Microglial Signaling Pathways

Permalink

https://escholarship.org/uc/item/0893q6c6

Journal

Translational Stroke Research, 14(4)

ISSN

1868-4483

Authors

Puglisi, Chloe H
Ander, Bradley P
Peterson, Catherine
et al.

Publication Date

2023-08-01

DOI

10.1007/s12975-022-01061-0

Peer reviewed

Sustained ICP Elevation Is a Driver of Spatial Memory Deficits After Intraventricular Hemorrhage and Leads to Activation of Distinct Microglial Signaling Pathways

Chloe H. Puglisi[1], **Bradley P. Ander**[2], **Catherine Peterson**[1], **Janet A. Keiter**[1], **Heather Hull**[2], **Cameron W. Hawk**[1], **Venina S. Kalistratova**[1], **Ali Izadi**[1], **Gene G. Gurkoff**[1], **Frank R. Sharp**[2], **Ben Waldau**[1]

[1]Department of Neurological Surgery, University of California at Davis Medical Center, 4860 Y Street, ACC 3740, Sacramento, CA 95817, USA

[2]Department of Neurology, University of California at Davis Medical Center, 4860 Y Street, ACC 3700, Sacramento, CA 95817, USA

Abstract

The mechanisms of cognitive decline after intraventricular hemorrhage (IVH) in some patients continue to be poorly understood. Multiple rodent models of intraventricular or subarachnoid hemorrhage have only shown mild or even no cognitive impairment on subsequent behavioral testing. In this study, we show that intraventricular hemorrhage only leads to a significant spatial memory deficit in the Morris water maze if it occurs in the setting of an elevated intracranial pressure (ICP). Histopathological analysis of these IVH + ICP animals did not show evidence of neuronal degeneration in the hippocampal formation after 2 weeks but instead showed significant microglial activation measured by lacunarity and fractal dimensions. RNA sequencing of the hippocampus showed distinct enrichment of genes in the IVH + ICP group but not in IVH alone having activated microglial signaling pathways. The most significantly activated signaling pathway was the classical complement pathway, which is used by microglia to remove synapses, followed by activation of the Fc receptor and DAP12 pathways. Thus, our study lays the groundwork for identifying signaling pathways that could be targeted to ameliorate behavioral deficits after IVH.

Keywords

Intraventricular hemorrhage; Intracranial pressure; Memory; Microglia; Complement activation; Fc receptor

Introduction

Intraventricular hemorrhage (IVH) is easily recognized with modern imaging but associated with a high mortality rate [1-3]. IVH is defined as an accumulation of blood within the ventricles of the brain and may be caused by intraventricular rupture of a parenchymal hemorrhage, a ruptured aneurysm/arteriovenous malformation, or traumatic brain injury [4, 5]. Additionally, IVH is also frequently seen in the setting of aneurysmal subarachnoid hemorrhage (SAH) which is known to cause subsequent cognitive dysfunction, problems with executive function, and memory deficits in some patients resulting in a large socioeconomic burden [6-8]. Good outcomes after IVH have been shown to be inversely proportional to the amount of intraventricular blood [9].

The impact of IVH and SAH on memory dysfunction has been well established, but the underlying mechanisms of memory loss have yet to be defined. Previously suggested mechanisms include hydrocephalus, blood toxicity, and neuroinflammation involving a proinflammatory response at the cellular level [4, 10, 11]. We have previously shown that microglia in the hilus of the rodent dentate gyrus become significantly more activated following IVH [12]. There is a wealth of animal studies exploring the cause of memory decline after non-traumatic intracranial hemorrhage, but studies examining the influence of elevated intracranial pressure (ICP) on memory decline are under-represented in the current literature [13].

Cognitive dysfunction after SAH has been difficult to simulate in rodent models since animals in some models showed either no or only mild cognitive deficits [14, 15]. Likewise, we have struggled in the past with obtaining reproducible behavioral deficits in a rat model of IVH. In this study, we show that introduction of rigorous ICP monitoring and sustained elevation of ICP in the setting of IVH induces a long-term spatial memory deficit and hydrocephalus in rats. Our model was supported by hippocampal gene expression analyses which showed a unique gene enrichment signature only in the IVH + ICP group and not in the IVH without elevated ICP group. Our data point towards involvement of microglial regulatory pathways in the memory dysfunction, opening avenues for targeting these pathways in the future to ameliorate cognitive deficits after IVH.

Materials and Methods

Animal Surgery

All animal use protocols and procedures were approved by the Institutional Animal Care and Use Committee (IACUC) of the University of California Davis (protocol #21874). All procedures followed the ILAR Guide for the Care and Use of Laboratory Animals, IACUC policy on Surgery Guidelines for Rodents and the UC Davis Animal Welfare Assurance in compliance with the US Public Health Service. Male Sprague–Dawley rats

aged 8–20 weeks (ENVIGO, Livermore, CA) weighing 300–400 g were used for the study. Animals were anesthetized with 4% isoflurane (Henry Schein Animal Health, Dublin, OH) in an induction chamber and then intubated. Animals were ventilated, and anesthesia was maintained using 1–3% isoflurane and O_2/N_2 (1:2) carrier gas in a stereotaxic frame (Kopf Instruments, Tujunga, CA). Animal body temperature was monitored and kept at 37 °C using a rectal probe and electric heating pad. A 2-cm midline cranial incision was made exposing the skull and 2 ventricular burr holes were drilled. A 22-gauge ventricular cannula was stereotactically placed (coordinates: 1.4 medial–lateral, − 0.9 anterior–posterior, − 4.6 dorsal–ventral from bregma) in the right burr hole, and a 28-gauge ventricular needle was inserted into the right ventricle (Plastic One Inc. Roanoke, VA). Subsequently, a 30-gauge ICP probe (OPP-M200 Fiber Optic Miniature Pressure Sensor, OpSens Medical, Québec, Canada) was placed 2 mm deep into the contralateral burr hole (− 1.4 medial–lateral, − 0.9 anterior–posterior, − 4.6 dorsal–ventral from bregma) to allow for continuous ICP monitoring.

The left femoral artery was dissected and cannulated to draw 0.2 ml of blood used for autologous ventricular hemorrhage. A 1.5–2.5 cm incision was made in the inguinal region of the left hind limb. The femoral artery was isolated, then a distal ligation and proximal aneurysmal clip were placed to halt blood flow for cannulation. A small incision was made near the distal suture, and a silastic tube was inserted into the artery. Two hundred microliters of arterial blood was collected in a syringe, and the proximal end of the artery was ligated. Subsequently, autologous blood was manually injected, using a pulsing thumb, into the right lateral cerebral ventricle over 2 min. During the 2-min injection, ICP data was collected using SoftSens (OpSens Medical, Québec, Canada) and graphically displayed to obtain baseline and maximum ICP values. After 10 min, the cranial needle was removed, and both incisions were closed using interrupted sutures. Once ambulatory, animals were returned to their home cages and provided ad libitum access to food and water. We observed no impairment of motor function in the left hind limb where the femoral artery had been ligated. Animals were euthanized if they lost more than 20% of their weight post-operatively.

Experimental Groups

Animals were divided into 4 main experimental groups: IVH + ICP, IVH, volume control, and sham control. The IVH + ICP animals received 200 μl of arterial autologous blood manually injected, using a pulsing thumb, over 2 min followed by artificial cerebrospinal fluid (aCSF, Baxter Healthcare Corporation, Deerfield, IL) mechanically pumped using a Hamilton syringe pump (Hamilton Company, Reno, NV) to bring the ICP to 50 mmHg which was then sustained for 2 h ($n = 12$). The average volume of aCSF that needed to be infused in the IVH + ICP group to keep the ICP around 50 mm Hg for 2 h was between 0.3 and 1.0 ml. The IVH group received 200 μl of autologous arterial blood manually injected, using a pulsing thumb, over 2 min ($n = 12$). The volume control group received 200 μl of aCSF manually injected, using a pulsing thumb, over 2 min ($n = 12$). Finally, the sham group received no fluid injection, but the cranial needle was inserted for 2 min and withdrawn ($n = 12$). All injections were into the right lateral ventricle. All animals recovered for 7 days. They were then tested on the Morris water maze on days 8–13. During the post-operative

period, 5 animals from each group underwent magnetic resonance imaging (MRI) scans. Animals were then euthanized via paraformaldehyde perfusion or decapitation 2–3 weeks after injury and within 1 week after the Morris water maze. Tissue collected following perfusion was used for histological analysis of the hippocampus. Fresh hippocampal tissue collected following decapitation was used for RNA sequencing. Separate cohorts of animals underwent injection of 300 μl of autologous arterial blood (IVH300; $n = 3$) and 400 μl of autologous arterial blood (IVH400; $n = 3$) and were compared to sham control animals. Another separate cohort of animals underwent a sustained elevation of ICP to 50 mm Hg for 2 h with the Hamilton syringe pump alone without the initial injection (ICP50; $n = 10$) and was compared to a new group of concurrently operated sham control animals ($n = 10$). Water maze experiments for the latter cohort were performed at the Rodent Behavior Core at UC Davis.

ICP Recordings

For each animal, maximum ICP values were recorded during the 2-min hand-pulsed injection period. Additionally, ICP values were recorded in 5-s intervals during the 2-min hand-pulsed injection period and 1.5 min before and after this period. These values were analyzed using Prism GraphPad (version 9.2.0 GraphPad Software, San Diego, CA) to generate an ICP graph for each animal which was then integrated to calculate the area under the curve to obtain the cumulative ICP over time integral during the ICP spike.

Morris Water Maze

To assess spatial learning acquisition and place recall memory, 48 experimental animals underwent Morris water maze testing 8–13 days post-op. The test was set up as follows: a large white tank (183 cm in diameter and 60 cm tall) was filled to 23 cm deep with water, and a transparent cylinder (12.8 cm in diameter, and 20 cm tall) was submerged to 3 cm into the second quadrant of the water. Water temperature was maintained at 26 °C ± 2 °C. On each wall surrounding the tank, there were unique shapes to provide spatial cues while animals navigated the tank searching for the submerged platform. Animals were given 5 training days to learn the location of the platform. Each training day consisted of 4 trials during which the animal was placed in the pool at a random starting location (North, South, East, West) and then given 120 s to find the platform, with 4-min breaks in-between trials. When the animals found the platform, they were allowed 30 s to remain on the platform before being removed from the pool. If the animal did not find the platform after 120 s, the experimenter would manually guide them to the platform and again allow them to remain on the platform for 30 s. Latency to reach the platform was recorded for each trial. On day 6, the submerged platform was removed from the tank, and animals were allowed 60 s to swim for the probe trial. From the probe trial, latency to first platform zone entry, swim speed, and time spent in the 10% and 5% (of the total tank area) circular area around the platform were recorded [16]. Animals were held in a warm cage between trials. Experimenters were blinded to experimental groups. Each trial was recorded using an overhead camera (Logitech Webcam software, Newark, CA) and later analyzed with a tracking software (AnyMaze version 6.0, Stoelting Co. Wood Dale, IL). To assess learning, mean latency across the 4 trials was calculated for each training day.

Corticosterone Analysis

To identify any relationship between intraventricular hemorrhage–related stress and memory deficits, we analyzed blood samples collected pre-injury, post-injury, and 2–3 weeks after injury before the decapitation. Five animals from IVH + ICP, IVH, and sham groups were randomly selected to be analyzed. Using the silastic tubing used to cannulate the artery and a 3-way stop-cock, 600 μl of blood was collected immediately before and after the intraventricular injection of 200 μl of blood. The final blood sample was collected 2–3 weeks after injury from the carotid artery just prior to tissue collection (post-injury week 2–3). Samples were analyzed at the UC Davis Nutrition department using an RIA corticosterone kit (MP Biomedicals, Orangeburg, NY).

MRI and Ventricular Measurements

To visualize the impact of intraventricular injections and sham surgery on the lateral ventricle, 5 animals from each main experimental group underwent MRI 1–5 days post-op. Animals were anesthetized with 3–5% isoflurane in a chamber and then maintained in the imaging instrument with 1–2% isoflurane and O_2 using nose cones. Body temperature and respiratory rates were monitored using a rectal thermometer connected to a physiological monitoring unit (SA Instruments, Stony Brook, NY). MRI scans were performed at the UC Davis Center for Molecular and Genomic Imaging on a Biospec 7 T MRI scanner (Brunker Biospin Corporation, San Jose, CA). Fifty-nine coronal images were produced with a field view of 35 mm × 25 mm using a T2 fast spin-echo sequence (repetition time/echo time = 6250/33 ms; bandwidth 39,062 Hz) with 8 echos at 11 ms apart and 4 averages. Image voxel size was 0.125 mm × 0.125 mm × 0.5 mm. To measure lateral ventricular volumes, MR images were analyzed by a blind observer using ImageJ [17]. On each coronal slice, both lateral ventricles were outlined, their areas summed, and then multiplied by section thickness (0.5 mm) to calculate total bilateral ventricular volumes.

RNA Isolation

Hippocampi were carefully dissected from the rat brains between 2 and 3 weeks following the initial surgery which is less than 1 week after the end of the Morris water maze testing. Total RNA was isolated using Zymo Direct-zol RNA Miniprep Plus according to the tough-to-lyse sample protocol (Zymo Research, Irvine, CA). Samples were kept frozen on dry ice while being weighed. A volume of TRI Reagent was added to a clean glass Dounce homogenizer proportional to the weight of the sample and placed on ice. The frozen sample was then added to the TRI Reagent using clean, frozen tweezers, and homogenization was completed over ice. Samples were homogenized until there were no visual solids observed and the lysate was transparent (about 20 passes). The lysate was then transferred to a tube and centrifuged for 1 min at 10,000 × g. The supernatant was then removed and transferred to a new nuclease-free tube and RNA purification completed. DNase 1 treatment was performed, and samples were eluted in 50 μl DNase/RNase free water. Eluted RNA was quantified using the NanoDrop 2000 Spectrophotometer (Thermo Fisher Scientific, Waltham, MA) and Qubit 3 Fluorometer using the Qubit High Sensitivity RNA Assay Kit (LifeTechnologies, Carlsbad, CA). The quality of eluted RNA was assessed using Agilent 2100 Bioanalyzer system with the RNA 6000 Nano Kit (Agilent Technologies, Inc., Santa

Clara, CA). One IVH + ICP sample failed quality checks reducing the group size by one. Eluted RNA was stored at − 80 °C.

RNA Libraries and Sequencing

Standard manufacturer protocol was used to generate libraries from 35 ng of total RNA targeting polyadenylated RNA using the QuantSeq 3' mRNAseq FWD protocol (Lexogen, Inc., Greenland, NH). Briefly, oligodT primers were used for reverse transcription followed by degradation of the original RNA strand. Second strand synthesis uses random priming and DNA polymerase and is followed by clean-up by magnetic beads. Illumina-compatible linker sequences were contained within the primer sequences and unique dual indices were introduced during PCR amplification. The fragment size distribution of the libraries was verified via micro-capillary gel electrophoresis on a LabChip GX system (PerkinElmer, Waltham, MA). The libraries were quantified by fluorometry on a Qubit fluorometer (LifeTechnologies) and pooled in equimolar ratios. The library pool was Exo-nuclease VII (New England Biolabs, Ipswich, MA) treated, SPRI-bead purified with KapaPure beads (Kapa Biosystems/Roche, Basel, Switzerland), and quantified via qPCR with a Kapa Library Quant kit (Kapa Biosystems) on a QuantStudio 5 RT-PCR system (Applied Biosystems, Foster City, CA). Final libraries were sequenced to 13.3 M ± 1.0 M single-end 85 base-pair reads on an Illumina NextSeq500 (Illumina, Inc., San Diego, CA).

Data Processing and Statistical Analysis

Raw FASTQ files were processed at the Linux command line according to standard protocols for Lexogen QuantSeq FWD data. Briefly, unique molecular identifier (UMI) tags were first moved to the read header and then samples aligned and annotated to the rat genome (Ensembl mRatBN7.2, annotation 105) using STAR 2.7.9a [18]. Aligned reads (BAM files) were then collapsed by UMI to produce gene counts, which were imported to Partek Flow (Partek, Inc., St. Louis, MO). Raw gene counts were normalized by the trimmed mean of m-values (TMM) before gene-specific analysis to test significance for differential expression. Differentially expressed genes (DEGs) were those called at $p <$ 0.05 and fold-change $>|1.2|$. Functional analysis of DEGs was performed in WEB-based GEne SeT AnaLysis Toolkit [19] through overrepresentation of gene lists against KEGG, Reactome, and WikiPathways databases.

Immunohistochemistry

Two to 3 weeks after surgery, animals were anesthetized and underwent trans-cardiac perfusion with 1x phosphate-buffered saline followed by 4% paraformaldehyde. Brains were removed, serially dehydrated in sucrose, then stored and snap-frozen in 30% sucrose. Five animals from each group were randomly selected, 40 μm coronal sections were cut using a cryostat (Leica CM1900, Leica Microsystems Inc., Bannockbum, Il) and then stained for NEUN, IBA1, CD68, CD74, C1Q, C3, Doublecortin (DCX), and Synaptophysin (SYP). The NEUN staining protocol is described in the Supplemental Methods.

To elucidate the relationship between IVH and microglia activation, fluorescent IBA1 staining was used. Every fifth coronal section (between plates 27 and 32) was mounted on SuperFrost Plus slides and allowed to air dry. The tissue was then circled with a PAP

pen and washed in PBS. Next, tissue was blocked in horse block (10% horse serum, 0.3% TritonX-100 in PBS) for 60 min at room temperature. Subsequently, tissue was incubated in primary antibody for 48 h at 4 °C (Rabbit anti-IBA1, Wako, 019–19,741, 1:500). Afterwards, tissue was washed in PBS before incubation in secondary antibody for 60 min at room temperature (Alexa Fluor 647 donkey anti-Rabbit, Invitrogen, A21206, 1:500). Finally, the tissue was washed in PBS and rinsed in double-distilled H_2O before it was coverslipped with Fluoromount G (Southern Biotech, Birmingham, AL) [12]. Fractal and lacunarity analysis methods are described in the Supplemental Methods.

Staining to mark CD68 receptors on the surface of activated microglia was optimized from a previously published protocol [20, 21]. The tissue was mounted on SuperFrost Plus slides and allowed to air dry. Then, slides were washed in PBS-Triton for 15 min, subsequently washed in PBS, and blocked for 1 h at room temperature (10% NGS + 1% BSA + 0.3% TritonX-100 in PBS) before incubation in primary antibody for 48 h at 4 °C (mouse anti-rat CD68, Bio-Rad Laboratories (Hercules, CA), MCA341GA, 1:200, Rabbit anti-IBA1, Fujifilm Wako (Osaka, Japan), 019–19,741, 1:500). Next, slides were washed in PBS and incubated in secondary antibody for 1.5 h at room temperature (Alexa Fluor goat anti-mouse, Invitrogen (Waltham, MA), A11005, 1:500, Alexa Fluor goat anti-rabbit 488, Molecular Probes (Eugene, OR), A11008, 1:500). Finally, slides were washed in PBS and then air-dried and coverslipped with Fluoromount G. Similarly, staining to identify CD74 and receptors on the surface of activated microglia was performed. In brief, tissue was mounted on SuperFrost Plus slides and allowed to air dry. Slides were washed in PBS, blocked for 1 h at room temperature (10% NGS + 1% BSA + 0.3% TritionX-100), and then incubated in primary antibody for 24 h at 4 °C (mouse anti-CD74, Bio-Rad Laboratories (Hercules, CA), MCA46R, 1:25, Rabbit anti-IBA1, Fujifilm Wako (Osaka, Japan), 019–19,741, 1:500). Next slides were washed in PBS and subsequently incubated in secondary antibody for 2 h at room temperature (donkey anti-mouse FITC, Jackson Immunoresearch (West Grove, PA), 715–095-151, 1:200, Alexa Fluor donkey anti-rabbit 555, Abcam (Cambridge, UK), ab150074, 1:1000). Finally, slides were washed in PBS then air-dried and coverslipped with Fluoromount G [22, 23]. Additionally, C1Q and C3 staining was performed to identify synapses tagged for microglial elimination as previously described [22-24]. The tissue was mounted on SuperFrost Plus slides and allowed to air dry. Next, slides underwent a heat-mediated antigen retrieval using EDTA + 0.2% Tween for 15 min. Slides were then washed in PBS, blocked for 1 h at room temperature, and incubated in primary antibody for 48 h at 4 °C (Rabbit anti-C3 recombinant EPR1934 Abcam (Cambridge, UK), ab200999, 1:200; Rabbit anti-C1Q recombinant EPR14634 Abcam, ab189922, 1:500). Next, slides were washed in PBS and subsequently incubated in secondary antibody for 1.5 h at room temperature (Alexa Fluor 488 donkey anti-rabbit Invitrogen (Waltham, MA), A-21206, 1:1000). Finally, slides were washed in PBS, air-dried, and coverslipped with Fluoromount G). To elucidate the location and function of complement components like C3 and C1Q, dual immunofluorescence was performed using IBA1, Synaptophysin, and Doublecortin (goat anti-IBA1, Abcam (Cambridge, UK), ab5076, 1:300, mouse anti-synaptophysin, Millipore (Darmstadt, Germany), MAB368, 1:500, mouse anti-DCX, Millipore (Darmstadt, Germany), MAB2253, 1:500) with respective secondary antibodies (donkey anti-goat Cy3, Jackson Immunoreseach (West Grove, PA), 705–16-147,

1:200, Alexa Fluor donkey anti-mouse 555, Invitrogen (Waltham, MA), ab150106, 1:1000, Alexa Fluor goat anti-guineapig 555, Invitrogen (Waltham, MA) A11075, 1:1000). Photomicrographs were taken using a fluorescent microscope (Zeiss LMS 800, Oberkochen, Germany), and images were processed with Zen imaging software (Zeiss, Oberkochen, Germany).

Statistical Analysis

Bilateral ventricular volumes were analyzed using one-way ANOVA and Bonferroni's multiple comparison correction test. Maximum ICP values were analyzed using a one-way ANOVA and post hoc Dunnett's test. ICP spike graphs were collected in SoftSens Software, integrated using GraphPad Prism, and analyzed using one-way ANOVA and post hoc Dunnett's test. Corticosterone levels were analyzed using repeated-measures ANOVA. Acquisition data collected from the Morris water maze was analyzed using a repeated-measures ANOVA with trial days as the repeated variable within subjects. Probe trial data for all groups except ICP50 including swim speed, latency to first platform zone entry, and time spent in the 5% and 10% concentric ring around the platform were analyzed using one-way ANOVA and post hoc Dunnett's test. Probe trial data for the ICP50 group com-ared to sham control was analyzed with an unpaired t-test. NEUN cell counts were compared between groups using a one-way ANOVA and a Dunnett's multiple comparison test. Summary data for fractal dimension and lacunarity was collected from the FracLac analysis, then cleaned and analyzed using custom scripts written in the open-source Python language and the freely available libraries, SciPy [25, 26]. We performed a Kruskal–Wallis H-test followed by a Mann–Whitney U-test with a Bonferroni correction for multiple comparisons, due to the non-parametric nature of the data as tested with Bartlett's test. A corrected p-value of less than 0.05 was considered significant.

Results

IVH Using Autologous Blood Caused ICP Spike

An overview of the experimental timeline of the in vivo experiments from surgery to tissue collection is provided in Fig. 1a. Figure 1b shows an example of an initial ICP spike to approximately 60 mm Hg during a 200 μl blood injection in an IVH + ICP animal followed by artificial elevation of the ICP to around 50 mm Hg by the infusion pump for 2 h. Figure 1c shows ICP recordings from a sham control animal. Note that the ICP during the introduction of the needle never exceeds 20 mm Hg. The ICP area under the curve was not significantly different for IVH + ICP vs IVH (p = 0.3668) or IVH + ICP vs volume control groups (p = 0.3888; Fig. 1d) showing that the initial injury was comparable among groups undergoing injections. There was a main effect of the group on ICP maximum spikes during hand-pulsed injections ($F_{(3, 36)}$ = 38.59). Animals from IVH + ICP (p < 0.0001), IVH (p < 0.0001), and volume control (p < 0.0001) groups had larger ICP maximum pressure spikes compared to sham animals (Fig. 1e), as expected. Maximum ICP spikes from IVH + ICP, IVH, and volume control groups showed no group effects ($F_{(2, 28)}$ = 2.197, p = 0.1300) indicating comparability of the initial injury between groups despite the use of different injectates (blood, aCSF). The effects of injury-related stress as a confounder on spatial memory were evaluated by analyzing the serum corticosterone concentration before, after,

and at the time of euthanasia. A mixed-model ANOVA showed a main effect of time but no significant group effect ($F_{(1.197, 14.36)} = 9.370$, $p = 0.0062$). These results suggest that the concentration of corticosterone decreased by post-injury days (PID) 14–17. However, there were no differences across groups at specific time points indicating that corticosterone levels did not change as a result of the intervention ($F_{(2, 12)} = 1.523$, $p = 0.2574$; Fig. 1f), and stress was likely not a confounder of behavioral testing. Interventions on average did not cause enough weight loss to lead to exclusion from the study (Online Resource 1).

Lateral Ventricular Volumes Increase After Sustained ICP Elevation

MR brain imaging was performed to evaluate animals for hydrocephalus. A one-way ANOVA comparing lateral ventricular volumes on MR images obtained 1–5 days after injury (for example, images see Fig. 2a-d) showed a significant group effect ($F_{(3, 16)} = 7.132$, $p = 0.0029$). Bonferroni's post hoc demonstrated that rats that underwent IVH + ICP had significantly larger ventricular volumes compared to sham control animals ($p_{adj} = 0.0019$, Fig. 2e). Ventricular volumes of IVH and volume control animals were not significantly affected compared to sham ($p_{adj} = 0.999$).

Only IVH with Sustained ICP Elevation Causes Deficits in Long-Term Spatial Memory

To determine if one of the groups had memory deficits, we tested whether there was a group effect on learning and memory 8–13 days after injection. A repeated-measures ANOVA yielded no significant difference between groups to find the platform during acquisition ($F_{(3, 16)} = 0.2133$, $p = 0.8857$; Fig. 3a). There was no group effect on swim speed during the probe trial ($F_{(3, 40)} = 0.6285$, $p = 0.6009$; Fig. 3b) indicating that ligation of the left femoral artery did not impair motor function. In the probe trial, we found a main effect of the group on latency to reach the platform ($F_{3, 42)} = 3.976$, $p = 0.0140$; Fig. 3c). Additionally, one-way ANOVA revealed a significant effect on the group when evaluating time spent in the 10% ring ($F_{(3, 42)} = 3.467$, $p = 0.0244$) and 5% ring ($F_{(3, 42)} = 4.765$, $p = 0.0060$) during the probe trial. A post hoc Dunnett's analysis revealed that the IVH + ICP group spent significantly less time in the 10% ring than the IVH ($p = 0.0216$) and the volume control groups ($p = 0.0240$; Fig. 3d), and the IVH + ICP group spent significantly less time in the 5% ring than the IVH group ($p = 0.0016$; Fig. 3e).

To determine if more blood would cause a spatial memory deficit since 200 μl of blood did not cause a deficit in the probe trial, we also analyzed Morris water maze data from animals who were injected intraventricularly with 300 μl (IVH300) or 400 μl of blood (IVH400) and compared these animals to sham surgery animals. There was again no signifi-ant difference between groups to find the platform during acquisition ($F_{(2, 16)} = 0.7871$, $p = 0.4720$; Online Resource 2a). Moreover, there was also no group effect of time to platform, time spent in the 10% ring, and time spent in the 5% ring during the probe trial ($F_{(2, 12)} = 1.079$, $p = 0.4567$; $F_{(2, 12)} = 0.408$, $p = 0.6738$; $F_{(2, 12)} = 0.164$, $p = 0.8503$, respectively; Online Resource 2b, c, d). This showed that even large volumes of intraventricular blood do not cause a long-term spatial memory deficit.

To further investigate the role of increased intracranial pressure, we analyzed Morris water maze data from animals who underwent pump infusion of aCSF to raise the ICP to 50 mm

Hg for 2 h without a preceding injection (ICP50). Again, there was no significant difference between groups to find the platform during acquisition ($F_{(1, 18)}$ = 1.932, p = 0.1685; Online Resource 3a). There was also no significant difference in time to platform, time spent in the 10% ring, and time spent in the 5% ring during the probe trial ($t(16)$ = 0.098, p = 0.9231, $t(16)$ = 0.7625, p = 0.4569, $t(16)$ = 0.3647, p = 0.7201, respectively; Online Resource 3b, c, and d). These results show that severely elevated ICP over 2 h alone was insufficient to cause a long-term spatial memory deficit in our rodent model.

Gene Expression Profiling of the Hippocampus

All gene expression data from the RNAseq analysis are available in Online Resource 4a-e and archived at Zenodo (https://doi.org/10.5281/zenodo.6395261). Gene expression was consistent between the experimental groups with distributions of the 12,655 detected gene counts similar across IVH + ICP (median = 21.4 CPM, Q1–Q3 = 4.1–71.2 CPM), IVH (median = 21.5 CPM, Q1–Q3 = 4.1–72.1 CPM), and sham controls (median = 21.6 CPM, Q1-–Q3 = 4.1–72.0 CPM). Many genes were differentially expressed in the dissected hippocampus between the groups. Between the IVH + ICP group and the IVH group, there were 311 differentially expressed genes (DEGs) of which 186 were expressed higher and 125 were lower in the IVH + ICP group compared to the IVH group (Online Resource 4a-e). There were 412 DEGs between the IVH + ICP group and sham control group, including 220 elevated and 192 decreased genes. The IVH versus the sham control group had 182 DEGs of which 92 were increased and 90 were decreased. Overall gene expression profiles of the 50 genes most differentially expressed across all groups were highly consistent within each experimental group indicating consistency of surgical or sham treatments (Fig. 4a). Unsupervised hierarchical clustering of the sham control and IVH samples were separated from the IVH + ICP samples at the highest branch of the dendrogram based on gene expression profiles (Fig. 4a).

Taking each list of DEGs and running them through ontological databases using the WebGestalt interface, func-ional pathways and processes related to these gene sets were identified with overrepresentation in the curated gene sets above the cutoff of FDR < 0.05 (FDR = Benjamini-Hochberg False Discovery Rate for multiple comparisons; Fig. 4b). Combining multiple databases in the analysis allowed accounting for nuances in the curated lists and reinforced pathways with similar memberships. For the DEGs in the IVH + ICP vs IVH comparison, 31 pathways were enriched with FDR < 0.05 and represented several main themes of complement pathway and immune activation (Fig. 4b, Online Resource 4f). The most enriched pathway was classical complement activation with an enrichment score (ES) of 21.2. Several other pathways related to complement activation, and the complement cascade was also significantly overrepresented. Many pathways related to innate and adaptive immunity were enriched. Among the top enriched pathways were also Fc receptor–related (FCGR activation (ES = 15.1), FCERI activation (ES = 11.9), and FCERI mediated MAPK activation (ES = 9.8)). DAP12 signaling and DAP12 interactions were enriched with ES of 12.3 and 10.1, respectively. Pathways that were enriched for the DEGs between IVH + ICP and sham control groups were fewer, but similar, and included complement, immune, and DAP12 pathways (Online Resource 4 g). Notably, the

DEGs between the IVH and sham control groups were not overrepresented in any queried pathways above the FDR < 0.05 threshold (Online Resource 4 h).

Individual gene expression plots of genes implicated in complement, microglial, and Lyn-associated pathways are displayed in Fig. 5a-o. In all cases, these selected genes had elevated expression in the IVH + ICP group compared to the sham control and/or the IVH group. Cell surface markers *Cd68, Cd74,* and *Cd53* were elevated 3.8-fold ($p = 0.007$), 3.7-fold ($p = 0.0004$), and 1.9-fold ($p = 0.0003$), respectively, in the IVH + ICP group compared to IVH group. Members of the C1 complex *C1qa* (1.4-fold, $p = 0.04$), *C1qb* (1.5-fold, $p = 0.01$), and *C1r* (1.8-fold, $p = 0.04$) were significantly increased in the IVH + ICP group compared to the IVH group. *C1qc* was increased 1.4-fold, but just outside the significance cutoff ($p = 0.051$). *C3, C2,* and *C4a* expression were increased 3.5-fold ($p = 0.001$), 2.1-fold ($p = 0.0009$), and 2.2-fold ($p = 0.04$), respectively, in the IVH + ICP hippocampus compared to IVH. *Trem2* was 2.2-fold ($p = 0.003$) higher in the IVH + ICP group than in the IVH group. *Fcer1g* was 2.0-fold increased ($p = 0.001$) in the IVH + ICP group compared to the IVH group. *Csf1r* expression was 1.6-fold higher ($p = 0.002$) in the IVH + ICP group compared to the IVH group. Src family kinases *Lyn* and *Hck* were 1.8-fold ($p = 0.0001$) and 1.9-fold ($p = 0.04$) greater, respectively, in the IVH + ICP group compared to the IVH hippocampus. None of the aforementioned genes were significantly different between the IVH and sham control groups. Genes implicated in other known dementia or neurodegenerative processes including *App, Psd95* (aka *Dlg4*), alpha-synuclein (*Snca*), netrin (*Ntn1*), and netrin receptor (*Dcc*) were not statistically different between any of the groups (Online Resource 5).

IVH Did Not Cause Acute Hippocampal Neurodegeneration

Next, to evaluate the impact of our intraventricular hemorrhage model on hippocampal neurons, we compared neuronal cell counts within the granular zone of the dentate gyrus, CA1, and CA3 across experimental groups (Fig. 6a). Stereological analysis using one-way ANOVA did not reveal any significant difference in the neuron counts between groups in the dentate gyrus ($F_{(3, 16)} = 0.3029$, $p = 0.8229$), CA1 ($F_{(3, 16)} = 0.8172$, $p = 0.5031$), or CA3 ($F_{(3, 16)} = 0.03077$, $p = 0.9924$) 2–3 weeks after injury (Fig. 6b). Therefore, there was no evidence to suggest that injection of 200 μl autologous blood, 200 μl of aCSF, or 200 μl injection of autologous blood followed by 2 h of ICP elevation caused significant neuronal death when evaluated 2–3 weeks after injury. These data also suggest the long-term spatial memory deficits in the IVH + ICP group were not due to hippocampal cell death at this time.

Sustained Increase of Intracranial Pressure Combined with IVH Accentuates Microglial Activation

Since there was a significant enrichment of genes involved in regulating microglial activity in the IVH + ICP group compared to other groups, we assessed changes in microglial morphology as a proxy for microglial activation using previously published methods [26].

Utilizing IBA1-positive immunofluorescent images, we measured the fractal dimension and lacunarity of isolated microglial cells in all groups (Fig. 6c-f). Fractal dimension analysis quantifies the overall complexity in morphology resulting in a value that ranges from 1 to 2,

where 1 is a straight line in one dimension, and 2 is a fractal with infinite complexity in two dimensions. In the case of fractal dimensions, we found statistically significant differences between all groups. IVH + ICP showed the greatest decrease in fractal dimension (median = 1.3719, Q1–Q3 = 1.3226–1.4186) compared to all other groups including sham (median = 1.42315, Q1–Q3 = 1.37875–1.462), volume control (median = 1.4092, Q1–Q3 = 1.3512–1.4655), and IVH (median = 1.42905, Q1–Q3 = 1.374025–1.4744; Fig. 6g). The lowest fractal dimension was measured in the IVH + ICP group indicating the most profound shift to an ameboid shape consistent with microglial activation.

In the case of lacunarity, we saw a statistically sig-ificant decrease in values for 3 groups when compared to the sham group. Whereas volume control ((median = 1.1718, Q1–Q3 = 1.017–1.3531), IVH (median = 1.16085, Q1–Q3 = 1.008425–1.323275), and IVH + ICP (median = 1.1671, Q1–Q3 = 1.0212–1.3288) were not statistically significantly different from each other, they were all different from the sham group (median = 1.21085, Q1–Q3 = 1.0655–1.3658; Fig. 6h). This decrease in lacunarity means that the microglia in these three groups exhibited increased radial symmetry around the center suggesting microglial activation as compared to sham which exhibited more directionally oriented microglia. Microglia showed no difference in fractal dimensions and lacunarity on the side of the injury compared to the contralateral hemisphere in the IVH + ICP group. This could suggest that the intracranial pressure is distributed evenly inside the calvarium in our model and/or the intraventricular blood is distributed evenly (Online resource 6).

Complement Staining Validates RNA Sequencing Results

Tissues from all four experimental groups showed colocalization of IBA1 and CD68 confirming proinflammatory microglial activation (Fig. 7a-d). Likewise, tissue from all four experimental groups showed colocalization of IBA1and CD74 (Fig. 7e-h). Representative images showed an increased expression of C1Q in the granule cell layer of the dentate gyrus in the IVH + ICP group compared to other groups (Fig. 7i-l). IVH + ICP histology also qualitatively showed an increased C3 expression in the subgranular zone and granule cell layer of the dentate gyrus compared to the other groups validating its 3.5-fold enrichment found in RNAseq experiments (Fig. 7m-p).

Activated Microglia Express Markers of a Proinflammatory M1 Phenotype, and C1Q Is Expressed Along Dendrites and Synapses

A further subanalysis of the RNAseq data revealed that a greater number of individual genes was associated with a proinflammatory (M1) rather than a non-inflammatory (M2) microglial phenotype (Fig. 8a) according to a previously published microglial classification scheme [27]. IVH + ICP animals exhibited C1Q expression near activated microglia in the SGZ of the dentate gyrus (Fig. 8b). This group of animals also demonstrated C1Q expression in alignment with the dendritic processes of newly generated dentate progenitor cells in the granular zone of the dentate gyrus (Fig. 8c). Finally, Synaptophysin (SYP) and C1Q showed colocalization in some areas of the SGZ of the dentate gyrus in the IVH + ICP group (white arrows, Fig. 8d) raising the possibility of incipient synaptic elimination.

Discussion

In this study, we show that IVH alone does not cause a significant long-term spatial memory deficit in rats, and spatial memory deficits only develop after raising the ICP to 50 mm Hg for 2 h in the setting of IVH. Our behavioral findings are supported by gene expression analyses which show that only in the setting of IVH + ICP rodents show activation of several microglial signaling pathways in the hippocampus, and IVH alone does not significantly activate these microglial signaling pathways.

Our findings challenge a large body of literature that implicates blood or thrombin alone as the culprit of memory deficits after intracranial hemorrhage (for a detailed review, see [13]). However, we believe that our findings align well with the clinical observation that patients often have good memory outcomes after SAH and IVH as long as they present to the hospital as a good clinical grade and do not have severe global cerebral edema and increased ICP [28]. In addition, many of the previous thrombin and hemoglobin studies did not control for intracranial pressure, so any role for elevated ICP in these models is uncertain. In addition, many different species of rats and mice were used in previous studies which could have contributed to variable results. We know that patients with IVH stemming from a ruptured aneurysm or intraventricular rupture of an intraparenchymal hemorrhage may develop increased ICPs requiring placement of an external ventricular drain (EVD) in the setting of hydrocephalus. Thus, it is not uncommon to see in clinical practice what we simulate in the rodent model presented in this study since IVH + ICP animals also developed hydrocephalus. We found activation of microglia in the hippocampus when assessing their fractal dimensions and lacunarity. It is unclear whether progressive hydrocephalus in IVH + ICP animals triggered microglial activation as seen in a model of inherited aqueductal stenosis [29] or whether elevated ICP activated microglia which subsequently caused hydrocephalus through ependymal cell damage or other pathways [30, 31]. On the other hand, sustained ICP elevation alone did not cause a long-term spatial memory deficit either so there likely is a role for the toxicity of blood to further trigger microglial activation and inflammatory pathways in the setting of high ICP.

Our gene expression analysis identified microglial activation pathways as a possible mechanism of the spatial memory decline. The data was very consistent since all IVH + ICP animals showed activation of key genes in microglial pathways whereas the other groups consistently showed no activation. Genes associated with dementia such as APP and alpha-synuclein were not activated in our model, so there is no evidence that IVH + ICP pushes the rodent brain towards pathways associated with classical dementias. Our data show that microglia may be a key component of the mechanism of spatial memory loss perhaps by stripping synapses in the hippocampus, which is supported in part by the most significant decrease in microglial fractal dimensions in the IVH + ICP group.

The most significantly activated pathway identified in our model is the classical complement activation pathway. C1Q is the initiating protein of this cascade and leads to down-stream accumulation of C3. Our pathway analysis showed that the classical complement pathway was the most significantly upregulated pathway after IVH + ICP compared to IVH alone, and all constituents of this pathway were upregulated. The classical complement pathway

mediates CNS synapse elimination through microglia [32]. Microglia are part of the physiological process of synapse removal in the brain through C3 binding with their C3 receptors if synapses are not used frequently [33]. C3-induced increased elimination of synapses in retinogeniculate neurons has been found in pathological conditions, such as glaucoma [32]. Interestingly, both glaucoma and our IVH + ICP model share increased pressure as a root cause of the problem. It is possible to imagine a similar mechanism in the dentate gyrus in the setting of elevated ICP. Microglia regulate forgetting through the elimination of synapses tagged with C3 on dendrites in the dentate gyrus [22]. We saw increased C3 expression in the subgranular zone and granule cell layer of the dentate gyrus and colabeling of C1Q with Synaptophysin raising the possibility that IVH + ICP leads to increased synaptic elimination on dendrites of the dentate gyrus. This hypothesis will require experimental confirmation. Further research is also needed to determine whether only IVH + ICP activates the classical complement pathway through the presence of blood since a separate cohort of animals with an isolated ICP elevation to 50 mm Hg over 2 h did not develop a long-term spatial memory deficit.

The second most significantly activated pathway in our IVH + ICP model compared to IVH was the Fc-epsilon receptor pathway. Fc receptors (FcRs) are part of the immunoglobulin (IgG) superfamily that attach to the constant domain (Fc) of Ig [34]. Fc-epsilon receptor binds IgE [35] and was significantly upregulated in our model. It is possible that our model increased the permeability of the blood–brain barrier due to high ICP and inadequate cerebral perfusion as seen in traumatic brain injury [36]. Thus, microglia may have become exposed to the Fc portion of leaked immunoglobulins inducing activation and subsequent dysfunction.

Finally, the third most significantly activated pathway was also linked to microglia with the TREM2 receptor pathway. TREM-2 receptors are mainly expressed on microglia [37] and are associated with DNAX activation protein 12 (DAP12, [37]). The activation of the receptor leads to overexpression of a tyrosine-kinase-based activation motif (ITAM) that results in chemokine production and reduction of a proinflammatory state [38]. We also saw an increased expression of calcium signaling in our pathway analysis, and TREM-2 has been shown to cause its effects by increasing calcium signaling through purinergic receptors [39].

Our finding that activation of the classical complement pathway is a key component of the injury opens the oppor-unity to develop targeted therapies to ameliorate outcomes after IVH + ICP in the setting of a ruptured brain aneurysm or hypertensive brain hemorrhage which can both be associated with elevated ICP. C1 activation, for example, may be inhibited with the administration of C1 esterase inhibitor CLH, a soluble glycoprotein, which has been shown to decrease inflammatory markers after myocardial ischemia–reperfusion injury [40, 41]. C3 receptors may be blocked with C3a receptor antagonist SB290157 which has been found to improve outcomes after ischemia [42]. FcRs could be blocked with IVIG or Fc receptor antibodies as shown previously [43, 44]. Finally, TREM-2 may have a beneficial effect on inflammation so its stimulation with a TREM-2 ligand may be beneficial [45].

In conclusion, we show in this study that ICP is the most important factor in causing a long-term spatial memory deficit in an IVH rodent model, and IVH alone, even with large

volumes of blood, does not cause a spatial memory deficit. IVH + ICP but not IVH alone was associated with the activation of distinct microglial signaling pathways such as the classical complement activation cascade, FcR and DAP12. These signaling pathways may be targeted in future interventions to prove causality and try to ameliorate memory deficits after IVH.

Supplementary Material

Refer to Web version on PubMed Central for supplementary material.

Acknowledgements

Funding

Data Availability

The datasets generated during the RNAseq analysis are available in Online Resource 4a-e and archived in the Zenodo repository (https://doi.org/10.5281/zenodo.6395261).

References

1. Wiggins WS, Moody DM, Toole JF, Laster DW, Ball MR. Clinical and computerized tomographic study of hypertensive intracerebral hemorrhage. Arch Neurol. 1978;35:832–3. [PubMed: 718487]

2. Angelopoulos M, Gupta SR, Azat Kia B. Primary intraventricular hemorrhage in adults: clinical features, risk factors, and outcome. Surg Neurol. 1995;44:433–6 (discussion 437). [PubMed: 8629227]

3. Steiner T, Diringer MN, Schneider D, Mayer SA, Begtrup K, Broderick J, et al. Dynamics of intraventricular hemorrhage in patients with spontaneous intracerebral hemorrhage: risk factors, clinical impact, and effect of hemostatic therapy with recombinant activated factor VII. Neurosurgery. 2006;59:767–73 (discussion 773–4). [PubMed: 17038942]

4. Bu Y, Chen M, Gao T, Wang X, Li X, Gao F. Mechanisms of hydrocephalus after intraventricular haemorrhage in adults. Stroke Vasc Neurol. 2016;1:23–7. [PubMed: 28959460]

5. Gaberel T, Magheru C, Emery E. Management of non-traumatic intraventricular hemorrhage. Neurosurg Rev. 2012;35:485–94 (discussion 494–5). [PubMed: 22732889]

6. Dodel R, Winter Y, Ringel F, Spottke A, Gharevi N, Müller I, et al. Cost of illness in subarachnoid hemorrhage: a German longitudinal study. Stroke. 2010;41:2918–23. [PubMed: 21071720]

7. Kreiter KT, Copeland D, Bernardini GL, Bates JE, Peery S, Claassen J, et al. Predictors of cognitive dysfunction after subarachnoid hemorrhage. Stroke Am Heart Assoc. 2002;33:200–9.

8. Al-Khindi T, Macdonald RL, Schweizer TA. Cognitive and functional outcome after aneurysmal subarachnoid hemorrhage. Stroke. 2010;41:e519–36. [PubMed: 20595669]

9. Tuhrim S, Horowitz DR, Sacher M, Godbold JH. Volume of ventricular blood is an important determinant of outcome in supratentorial intracerebral hemorrhage. Crit Care Med. 1999;27:617–21. [PubMed: 10199544]

10. Garton T, Hua Y, Xiang J, Xi G, Keep RF. Challenges for intraventricular hemorrhage research and emerging therapeutic targets. Expert Opin Ther Targets. 2017;21:1111–22. [PubMed: 29067856]

11. Mracsko E, Veltkamp R. Neuroinflammation after intracerebral hemorrhage. Front Cell Neurosci. 2014;8:388. [PubMed: 25477782]

12. Kamal K, Keiter JA, Binyamin TR, de la Cruz Dapula JN, Vergara AR, Hawk CW, et al. Mechanical injury and blood are drivers of spatial memory deficits after rapid intraventricular hemorrhage. Neurobiol Dis. 2020;145:105084. [PubMed: 32941979]

13. Peterson C, Umoye AO, Puglisi CH, Waldau B. Mechanisms of memory impairment in animal models of nontraumatic intracranial hemorrhage: a systematic review of the literature. Brain Hemorrhages [Internet]. 2021; Available from: https://www.sciencedirect.com/science/article/pii/S2589238X21000383

14. Milner E, Holtzman JC, Friess S, Hartman RE, Brody DL, Han BH, et al. Endovascular perforation subarachnoid hemorrhage fails to cause Morris water maze deficits in the mouse. J Cereb Blood Flow Metab [Internet]. 2014;34. Available from: 10.1038/jcbfm.2014.108

15. Regnier-Golanov AS, Gulinello M, Hernandez MS, Golanov EV, Britz GW. Subarachnoid hemorrhage induces sub-acute and early chronic impairment in learning and memory in mice. Transl Stroke Res [Internet]. 2022; Available from: 10.1007/s12975-022-00987-9

16. Garthe A, Behr J, Kempermann G. Adult-generated hippocampal neurons allow the flexible use of spatially precise learning strategies. PLoS ONE. 2009;4:e5464. [PubMed: 19421325]

17. Schneider CA, Rasband WS, Eliceiri KW. NIH image to ImageJ: 25 years of image analysis. Nat Methods. 2012;9:671–5. [PubMed: 22930834]

18. Dobin A, Davis CA, Schlesinger F, Drenkow J, Zaleski C, Jha S, et al. STAR: ultrafast universal RNA-seq aligner. Bioinformatics. 2013;29:15–21. [PubMed: 23104886]

19. Liao Y, Wang J, Jaehnig EJ, Shi Z, Zhang B. WebGestalt 2019: gene set analysis toolkit with revamped UIs and APIs. Nucleic Acids Res. 2019;47:W199–205. [PubMed: 31114916]

20. Noh J-E, Oh S-H, Park I-H, Song J Intracerebral transplants of GMP-grade human umbilical cord-derived mesenchymal stromal cells effectively treat subacute-phase ischemic stroke in a rodent model. Front Cell Neurosci. 2020;14:546659. [PubMed: 33100972]

21. Yousef H, Czupalla CJ, Lee D, Chen MB, Burke AN, Zera KA, et al. Aged blood impairs hippocampal neural precursor activity and activates microglia via brain endothelial cell VCAM1. Nat Med. 2019;25:988–1000. [PubMed: 31086348]

22. Wang C, Yue H, Hu Z, Shen Y, Ma J, Li J, et al. Microglia mediate forgetting via complement-dependent synaptic elimination. Science. 2020;367:688–94. [PubMed: 32029629]

23. Hwang IK, Park JH, Lee T-K, Kim DW, Yoo K-Y, Ahn JH, et al. CD74-immunoreactive activated M1 microglia are shown late in the gerbil hippocampal CA1 region following transient cerebral ischemia. Mol Med Rep. 2017;15:4148–54. [PubMed: 28487994]

24. He J-H, Liu R-P, Peng Y-M, Guo Q, Zhu L-B, Lian Y-Z, et al. Differential and paradoxical roles of new-generation antidepressants in primary astrocytic inflammation. J Neuroinflammation. 2021;18:4–7. [PubMed: 33402167]

25. Virtanen P, Gommers R, Oliphant TE, Haberland M, Reddy T, Cournapeau D, et al. SciPy 10: fundamental algorithms for scientific computing in Python. Nat Methods. 2020;17:261–72. [PubMed: 32015543]

26. Karperien A, Ahammer H, Jelinek HF. Quantitating the subtleties of microglial morphology with fractal analysis. Front Cell Neurosci. 2013;7:3. [PubMed: 23386810]

27. Jurga AM, Paleczna M, Kuter KZ. Overview of general and discriminating markers of differential microglia phenotypes. Front Cell Neurosci. 2020;14:198. [PubMed: 32848611]

28. Sanchez B, Delemos CD, Sandhu KS, Peterson C, Cord BJ, Gurkoff GG, et al. Aneurysmal subarachnoid hemorrhage survivors show long-term deficits in spatial reference memory in a pilot study of a virtual water maze paradigm. Clin Neurol Neurosurg. 2021;207:106788. [PubMed: 34230004]

29. Mangano FT, McAllister JP 2nd, Jones HC, Johnson MJ, Kriebel RM. The microglial response to progressive hydrocephalus in a model of inherited aqueductal stenosis. Neurol Res. 1998;20:697–704. [PubMed: 9864733]

30. Wu K-Y, Tang F-L, Lee D, Zhao Y, Song H, Zhu X-J, et al. Ependymal Vps35 promotes ependymal cell differentiation and survival, suppresses microglial activation, and prevents neonatal hydrocephalus. J Neurosci Soc Neurosci. 2020;40:3862–79.

31. Fernández-Arjona MDM, León-Rodríguez A, López-Ávalos MD, Grondona JM. Microglia activated by microbial neuramini-dase contributes to ependymal cell death. Fluids Barriers CNS. 2021;18:15. [PubMed: 33757539]

32. Stevens B, Allen NJ, Vazquez LE, Howell GR, Christopherson KS, Nouri N, et al. The classical complement cascade mediates CNS synapse elimination. Cell. 2007;131:1164–78. [PubMed: 18083105]

33. Schafer DP, Lehrman EK, Kautzman AG, Koyama R, Mardinly AR, Yamasaki R, et al. Microglia sculpt postnatal neural circuits in an activity and complement-dependent manner. Neuron. 2012;74:691–705. [PubMed: 22632727]

34. ElAli A, Rivest S. Microglia ontology and signaling. Front Cell Dev Biol. 2016;4:72. [PubMed: 27446922]

35. Daëron M Fc receptor biology. Annu Rev Immunol. 1997;15:203–34. [PubMed: 9143687]

36. Lin Y, Pan Y, Wang M, Huang X, Yin Y, Wang Y, et al. Blood-brain barrier permeability is positively correlated with cerebral microvascular perfusion in the early fluid percussion-injured brain of the rat. Lab Invest. 2012;92:1623–34. [PubMed: 22964852]

37. Colonna M TREMs in the immune system and beyond. Nat Rev Immunol. 2003;3:445–53. [PubMed: 12776204]

38. Fu R, Shen Q, Xu P, Luo JJ, Tang Y. Phagocytosis of microglia in the central nervous system diseases. Mol Neurobiol. 2014;49:1422–34. [PubMed: 24395130]

39. Jairaman A, McQuade A, Granzotto A, Kang YJ, Chadarevian JP, Gandhi S, et al. TREM2 regulates purinergic receptor-mediated calcium signaling and motility in human iPSC-derived microglia. Elife [Internet]. 2022;11. Available from: 10.7554/eLife.73021

40. Buerke M, Prufer D, Dahm M, Oelert H, Meyer J, Darius H. Blocking of classical complement pathway inhibits endothelial adhesion molecule expression and preserves ischemic myocardium from reperfusion injury1. JPET. 1998;286:429–38.

41. D'Ambrosio AL, Pinsky DJ, Connolly ES. The role of the complement cascade in ischemia/reperfusion injury: implications for neuroprotection. Mol Med. 2001;7:367–82. [PubMed: 11474130]

42. Ducruet AF, Zacharia BE, Sosunov SA, Gigante PR, Yeh ML, Gorski JW, et al. Complement inhibition promotes endogenous neurogenesis and sustained anti-inflammatory neuroprotection following reperfused stroke. PLoS ONE. 2012;7:e38664. [PubMed: 22761695]

43. Bayry J, Misra N, Latry V, Prost F, Delignat S, Lacroix-Desmazes S, et al. Mechanisms of action of intravenous immunoglobulin in autoimmune and inflammatory diseases. Transfus Clin Biol. 2003;10:165–9. [PubMed: 12798851]

44. Remlinger J, Madarasz A, Guse K, Hoepner R, Bagnoud M, Meli I, et al. Antineonatal Fc receptor antibody treatment ameliorates MOG-IgG-associated experimental autoimmune encephalomyelitis. neurol neuroimmunol neuroinflamm [Internet]. 2022;9. Available from: 10.1212/NXI.0000000000001134

45. Deczkowska A, Weiner A, Amit I. The physiology, pathology, and potential therapeutic applications of the TREM2 signaling pathway. Cell. 2020;181:1207–17. [PubMed: 32531244]
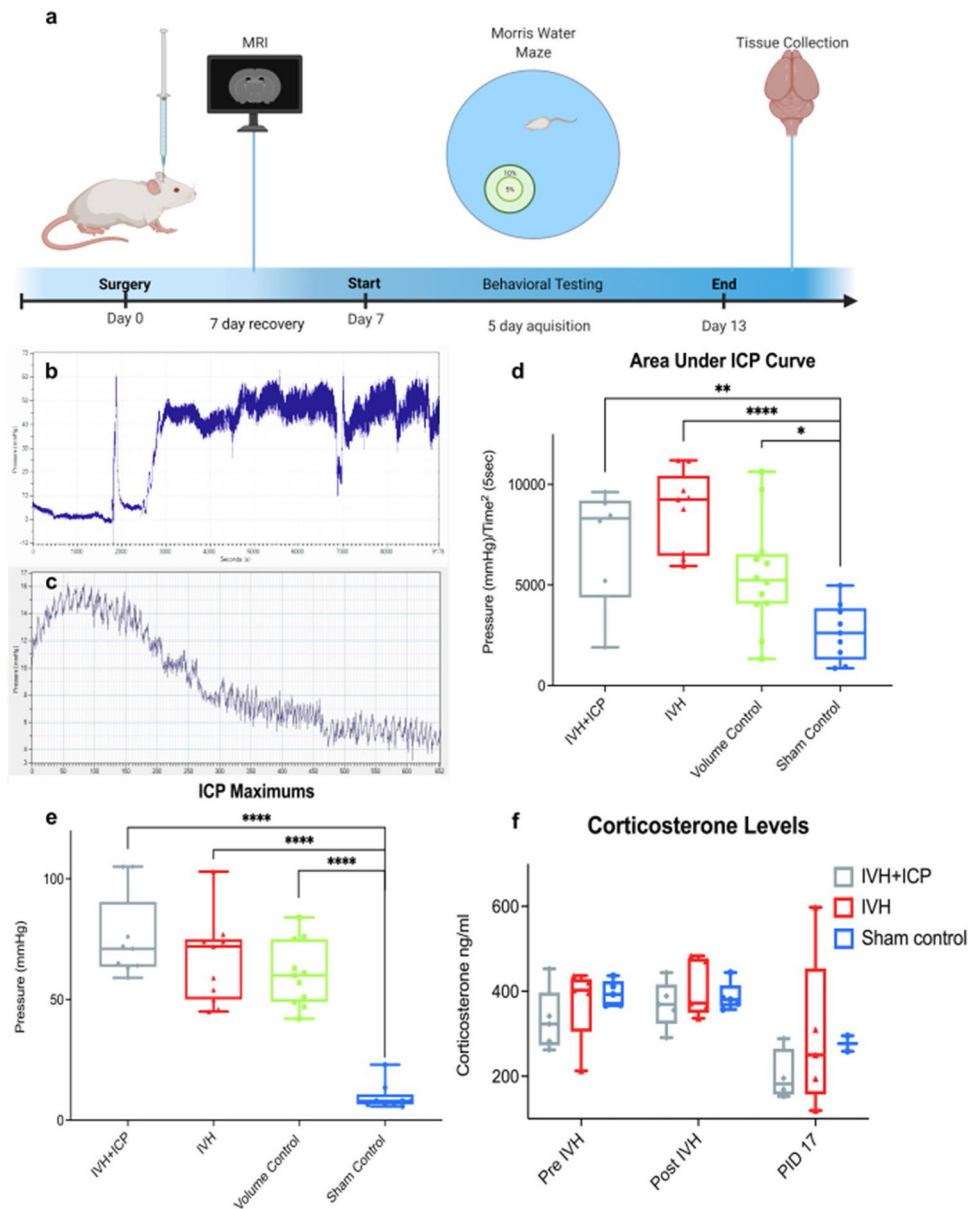
Fig. 1.

a Timeline of in vivo experimental workflow showing the generation and evaluation of the injury model. **b** Example of an ICP graph from an ICP + IVH animal obtained using a fiberoptic pressure sensor showing the initial injury around approximately 2000s followed by artificial elevation of ICP after approximately 3000 s for 2 h. **c** Example of an ICP graph from a sham control surgery animal showing no elevation of ICP above 20 mm Hg at any point in time. **d** Animals with intraventricular blood and sustained ICP elevation (IVH + ICP), intraventricular blood (IVH), and intraventricular aCSF (volume control) had significantly larger areas under the ICP curve compared to sham injections (Dunnett's multiple comparison test * = $p < 0.05$, ** = $p < 0.01$, **** = $p < 0.0001$). There were no significant differences between IVH + ICP, IVH, and volume control. **e** Animals with intraventricular blood and sustained ICP (IVH + ICP), intraventricular

blood (IVH), and intraventricular aCSF (volume control) had significantly higher maximum ICP spikes compared to sham control. **f** There were no significant differences between IVH + ICP, IVH, and volume control corticosterone levels at any given sampling time point. Corticosterone levels decrease post-operatively but were unchanged between groups indicating no differential stress response (whiskers: minimal and maximal values; boxes: interquartile range; bar: median)
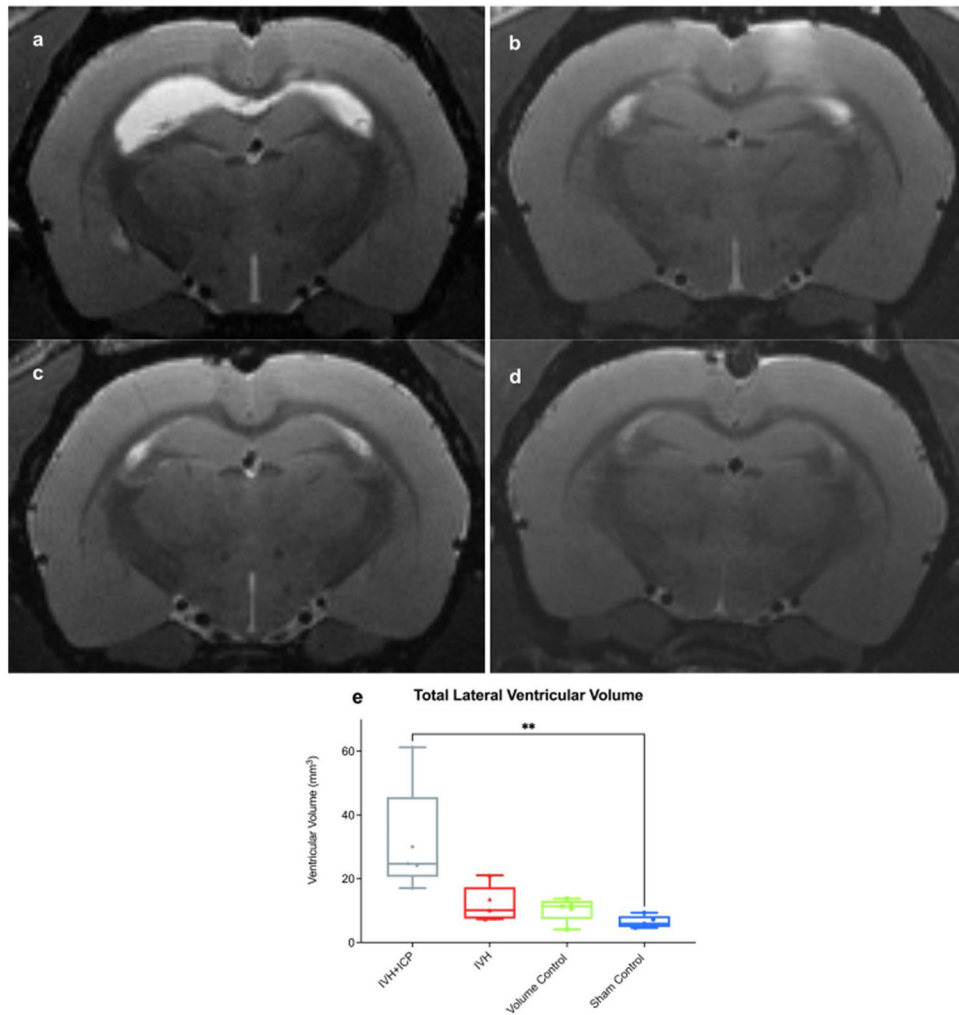
Fig. 2.

T2-weighted MRI brain scans 1–5 days after **a** IVH + ICP, **b** IVH, **c** artificial CSF (volume control), or **d** sham surgery. **e** Only pulsed thumb injections of blood followed by 2 h of ICP elevation to 50 mm Hg caused significantly larger lateral ventricular volumes compared to sham surgery 1–5 days after injury. Pulsed thumb injections of blood or aCSF did not significantly change lateral ventricular volumes compared to sham surgery (Dunnett's multiple comparison test ** = $p < 0.01$). Whiskers: minimal and maximal values; boxes: interquartile range; bar: median
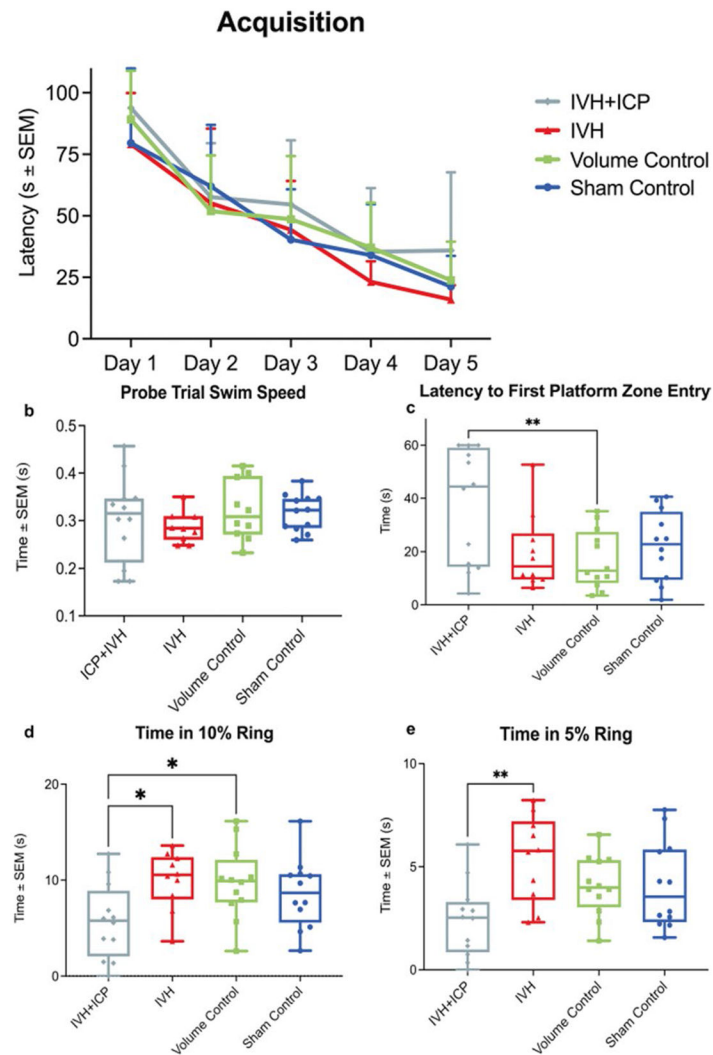
Fig. 3.

Acquisition learning of rats 8–13 days after intraventricular injections or sham surgery in the Morris water maze. **a** Repeated-measures ANOVA showed no difference during acquisition days between groups. **b** Average swim speeds during the probe trial were unchanged between groups. **c** During the probe trial, IVH + ICP animals took significantly longer to enter the area where the platform was located compared to volume control animals. **d** During the probe trial, animals with IVH + ICP spend significantly less time in the 10% area around the platform compared to IVH and volume control animals. **e** During the probe trial, animals with IVH + ICP spent significantly less time in the 5% area around the platform compared to IVH animals (Dunnett's multiple comparison test * = $p < 0.05$, ** = $p < 0.01$; whiskers: minimal and maximal values; boxes: interquartile range; bar: median)
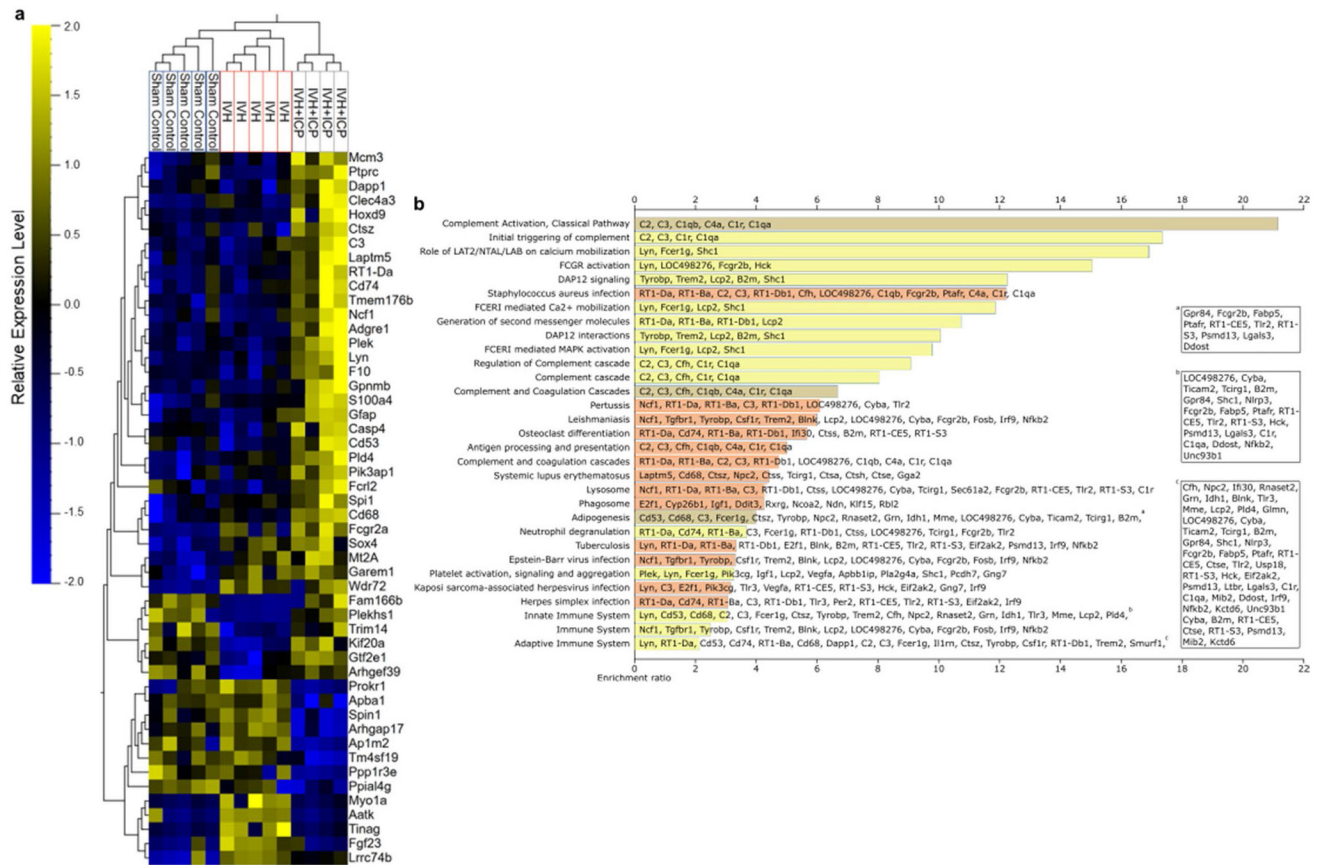
Fig. 4.

a Heatmap of the top 50 differentially expressed genes across the hippocampus of the IVH + ICP, IVH, and sham control rats. Unsupervised hierarchical clustering of the experimental groups (top) highlights the relatedness of the expression profiles within each group of animals and consistency of the surgical procedures. **b** The 31 enriched functional pathways overrepresented by the differentially expressed genes in the IVH + ICP vs the IVH group (FDR < 0.05). Enrichment score is plotted to the right of each pathway representing the fold enrichment of the pathway greater than the expected representation in the gene list. Member genes in the DEG list are included in the overlay of the enrichment score bars. Overflow of gene lists continue for adipogenesis, innate immune system, and adaptive immune system appear in the boxes denoted a, b, and c in the figure. Colors of the enrichment score bars indicate the database from which the pathways are curated: WikiPathways—light brown, KEGG—orange, and Reactome—yellow
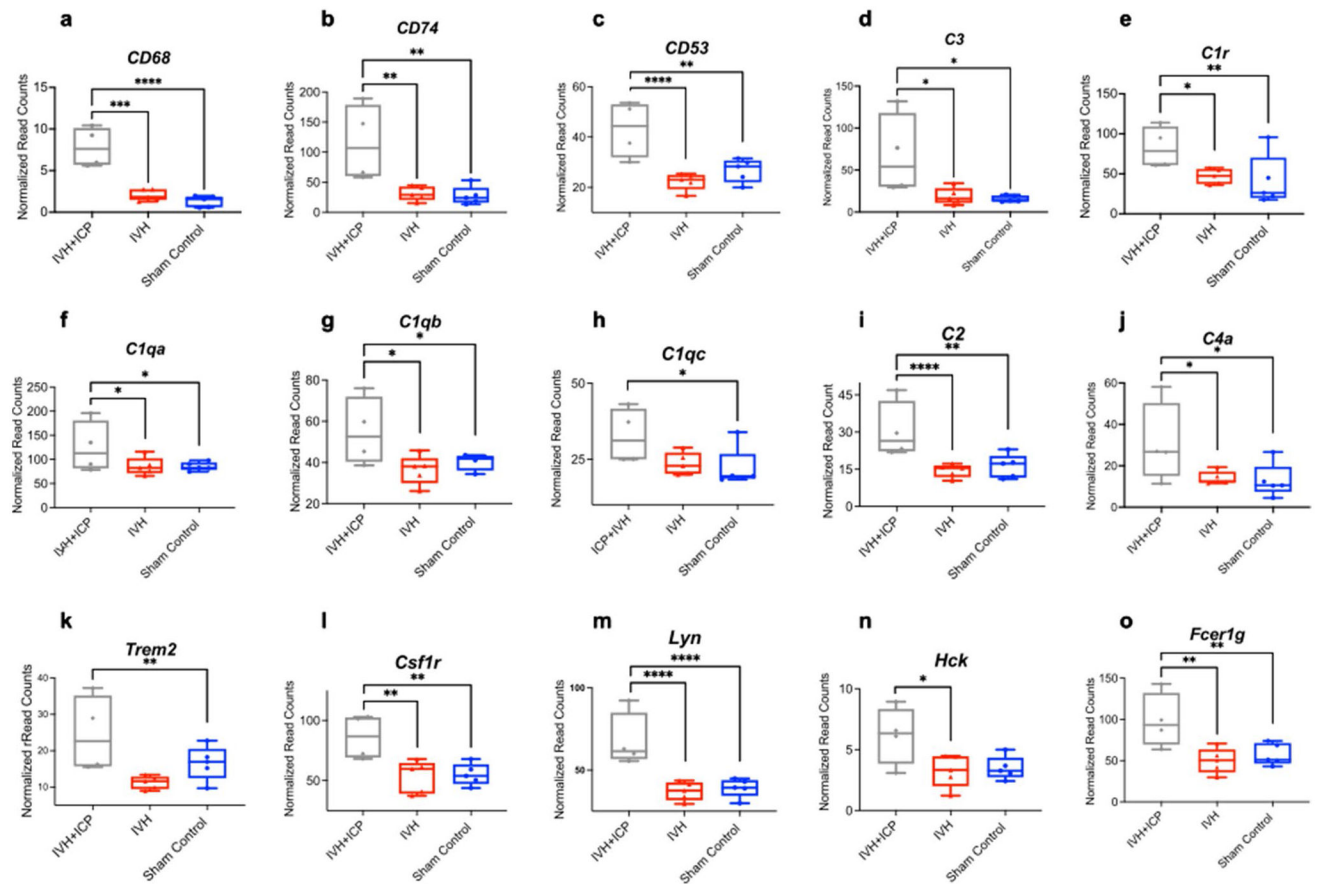
Fig. 5.
Expression levels of individual genes measured in the hippocampus of IVH + ICP, IVH, and sham control rats: **a** *Cd68*; **b** *Cd74*; **c** *Cd53*; **d** *C3*; **e** *C1r*; **f** *C1qa*; **g** *C1qb*; **h** *C1qc*; **i** *C2*; **j** *C4a*; **k** *Trem2*; **l** *Csf1r*; **m** *Lyn*; **n** *Hck*; and **o** *Fcer1g*. Statistical significance from analysis of the TMM data is shown between the indicated groups with * = $p < 0.05$, ** = $p < 0.01$, *** = $p < 0.001$, and **** = $p < 0.0001$. Values are presented in counts per million (CPM). (whiskers: minimal and maximal values; boxes: interquartile range; bar: median)
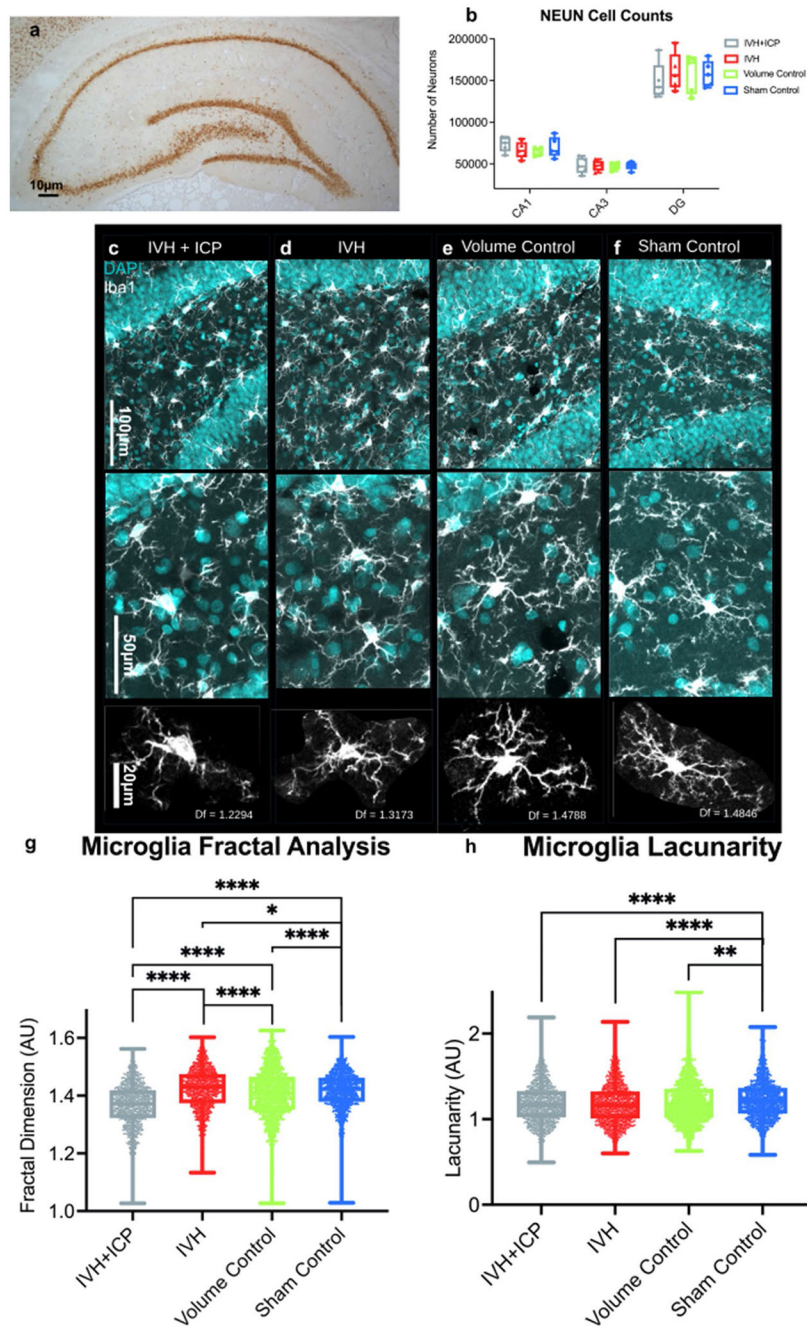
Fig. 6.

a NEUN staining of the hippocampal formation showed **b** no significant differences in neuronal cell counts between experimental groups 2–3 weeks after injury in CA1, CA3, and dentate gyrus regions using stereological counting methods. **c-f** Morphological analysis of microglia in all groups showed that **g** fractal dimensions were altered for all three injection groups compared to sham surgery, with IVH + ICP showing the most profound decrease in fractal dimensions and therefore the highest degree of microglial activation. **h** Lacunarity showed a similar decrease for all three experimental groups compared to sham surgery indicating that microglia exhibited altered, activated morphology (* = $p < 0.05$, ** = $p <$

0.01, *** = $p < 0.001$, **** = $p < 0.0001$; whiskers: minimal and maximal values; boxes: interquartile range; bar: median)
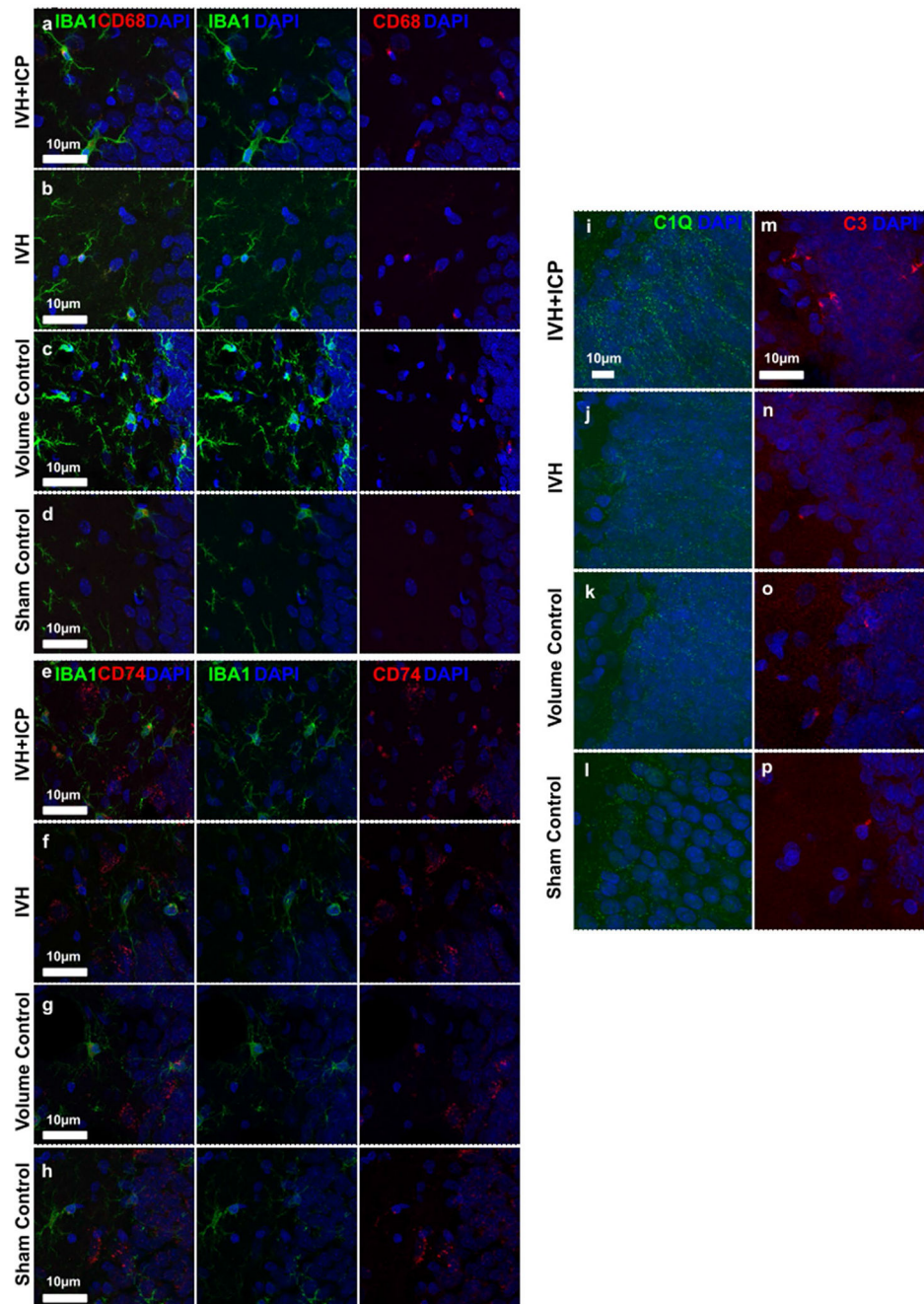
Fig. 7.
Representative images of CD68, CD74, and components of the classical complement cascade qualitatively validate RNAseq results. CD68-IBA1 is colocalized in the dentate gyrus of **a** IVH + ICP, **b** IVH, **c** volume control, and **d** sham control animals. Similarly, CD74-IBA1 is colocalized in the dentate gyrus of **e** IVH + ICP, **f** IVH, **g** volume control, and **h** sham control animals. Increased C1Q expression is observed in the granule cell layer of an **i** IVH + ICP animal compared to **j** IVH, **k** volume control, and **l** sham control animals. Increased expression of C3 is observed in the subgranular zone and granule cell layer of an **m** IVH + ICP animal compared to **n** IVH, **o** volume control, and **p** sham control animals
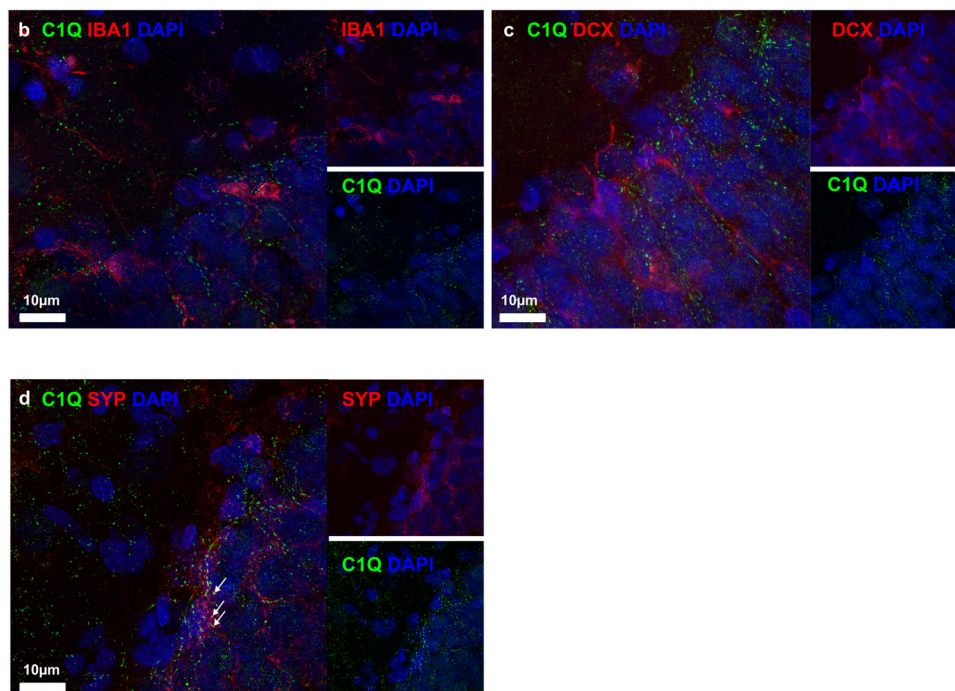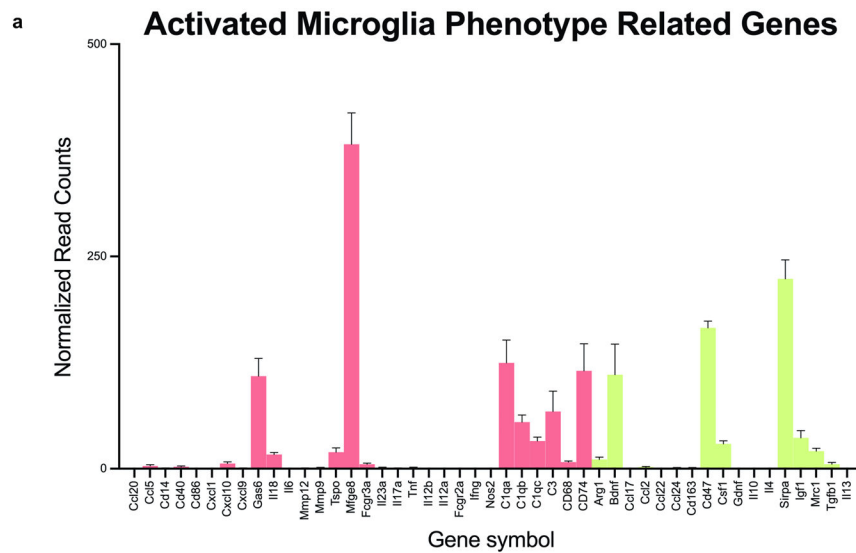
Fig. 8.
Expression of M1 and M2 phenotype–related genes suggests microglia are predominantly in an M1 proinflammatory activation state, and the proinflammatory marker C1Q is expressed in close proximity to microglia, dendrites, and synapses in IVH + ICP animals. **a** Genes associated with M1-activated proinflammatory microglial phenotypes (pink) outnumber genes associated with M2-activated non-inflammatory microglial phenotype (light green) based on a classification scheme published by Jurga et al. [27]. **b** C1Q and IBA1 label in close proximity to one another in the subgranular zone (SGZ) of the dentate gyrus in an IVH + ICP animal. **c** C1Q and Doublecortin (DCX) stain in parallel along the dendritic

projections in the granule cell layer of the dentate gyrus in an IVH + ICP animal. **d** C1Q colocalizes with Synaptophysin (SYP) in the SGZ of the dentate gyrus in an IVH + ICP animal (white arrows)